Theoretical study of the microwave spectrum of isotopologues of OCS–$(He)_2$

Hui Li, Yongdong Liu, Wolfgang Jäger, Robert J. Le Roy, and Pierre-Nicholas Roy

Abstract: The rovibrational energy levels (J = 0–3) and rotational spectra of seven isotopologues of the OCS–$(He)_2$ complex have been determined by numerically exact basis set calculations. The interaction energy is represented as a sum of two-body terms consisting of the OCS–He potential, which Howson and Hutson (*J. Chem. Phys.* **2001,** *115,* 5059) obtained at the CCSD(T)/aug-cc-pVTZ level of theory, and the He–He potential that Jeziorska et al. (*J. Chem. Phys.* **2007,** *127,*124303) obtained with SAPT theory. Three-body effects and the quality of the potential are discussed. Comparison with experiment shows that microwave transitions can be predicted by this additive approach with an accuracy equal or better than 0.7% for all the observed spectral lines. A method for the three-dimensional representation of the helium density in the body-fixed frame is presented that highlights the highly delocalized nature of the helium subsystem.

Key words: weakly bound clusters, quantum clusters, exact bound state calculations, microwave spectroscopy, rotational dynamics.

Résumé : Utilisant des ensembles de base numériquement exacts, on a calculé les niveaux d'énergie rovibrationnels (J = 0–3) et les spectres rotationnels de sept isotopologues du complexe OCS–$(He)_2$. L'énergie d'interaction est représentée par la somme de termes à deux corps formée du potentiel OCS–He que Howson et Hutson (*J. Chem. Phys.* **2001,** *115,* 5059)ont déterminé au niveau CCSD(T)/aug-cc-pVTZ de la théorie et du potentiel He–He que Jeziorska et al. (*J. Chem. Phys.* **2007,** *127,* 124303) ont déterminé à l'aide de la théorie des perturbations adaptée pour la symétrie (TPAS). On discute aussi des effets de trois corps et de la qualité du potentiel. Une comparaison des résultats des calculs avec des résultats expérimentaux montre que les transitions de microondes peuvent être mieux prédites par cette approche additive, avec une précision égale ou meilleure à 0,7 % pour toutes les raies spectrales observées. On présente une méthode de représentation tridimensionnelle de la densité de l'hélium dans un squelette à corps fixes qui est caractérisé par la nature hautement délocalisée du sous-système de l'hélium.

Mots-clés : agrégats faiblement liés, agrégats quantiques, calculs exacts de l'état lié, spectroscopie de microondes, dynamique rotationnelle.

[Traduit par la Rédaction]

Introduction

Doped helium clusters offer a unique opportunity to understand quantum solvation and microscopic superfluidity, and this topic has been the subject of several studies in recent years.[1–13] Helium clusters doped with carbonyl sulfide (OCS) are of particular interest, because the OCS chromophore was the dopant used to provide the first evidence of microscopic superfluidity in helium nanodroplets.[1] In that seminal work, it was found that the OCS molecule undergoes nearly free rotational motion with a renormalization of its moment of inertia owing to its coupling to the helium environment, and the nearly free nature of that rotational motion was attributed to superfluidity. Since that time, helium clusters doped with OCS have become the focus of numerous experimental and theoretical studies.[4,7,11,14–18] In particular, Xu and Jäger[3,6] and Tang and McKellar[4,7] have gone beyond the traditional binary or ternary complex limit to obtain infrared and microwave spectra of OCS–$(He)_N$ clusters for N = 2–8. In addition to being a technical breakthrough, that work hinted at the onset of superfluidity and provided benchmark challenges for theoretical studies.

To fully understand the experimental spectra on the atomic scale, computer simulation studies are important and necessary,[19,20] and a number of theoretical studies of OCS–$(He)_N$ clusters based on quantum Monte Carlo techniques have been reported.[14–18,21] Such techniques have also been applied to He clusters containing other dopants such as N_2O,[22,23] CO_2,[20,24,25] and HCCCN,[26] yielding excellent agreement with experiment. To date, however, exact quan-

Received 1 March 2010. Accepted 11 June 2010. Published on the NRC Research Press Web site at canjchem.nrc.ca on 4 November 2010.

This article is part of a Special Issue dedicated to Professor R. J. Boyd.

H. Li. Department of Chemistry, University of Waterloo, Waterloo, ON N2L 3G1, Canada; Institute of Theoretical Chemistry, State Key Laboratory of Theoretical and Computational Chemistry, Jilin University, 2519 Jiefang Road, Changchun 130023, P.R. China.
Y. Liu and W. Jäger. Department of Chemistry, University of Alberta, Edmonton, AB T6G 2G2, Canada.
R.J. LeRoy and P.-N. Roy.[1] Department of Chemistry, University of Waterloo, Waterloo, ON N2L 3G1, Canada.

[1]Corresponding author (e-mail: pnroy@uwaterloo.ca).

Fig. 1. Illustration of the coordinate system used in the bound-state calculations: M is the centre of mass of OCS and B is the canonical point for the Radau vectors $\mathbf{r}_1$ and $\mathbf{r}_2$, and $\mathbf{q}_1$ and $\mathbf{q}_2$ are the Jacobi vectors and $\mathbf{r}_0$ is a vector defining the axis of the OCS molecule; ϕ is a dihedral angle between $\mathbf{r}_1 \times \mathbf{r}_0$ and $\mathbf{r}_2 \times \mathbf{r}_0$, and θ_1 and θ_2 are angles between $\mathbf{r}_0$ and $\mathbf{r}_1$ and $\mathbf{r}_2$, respectively.

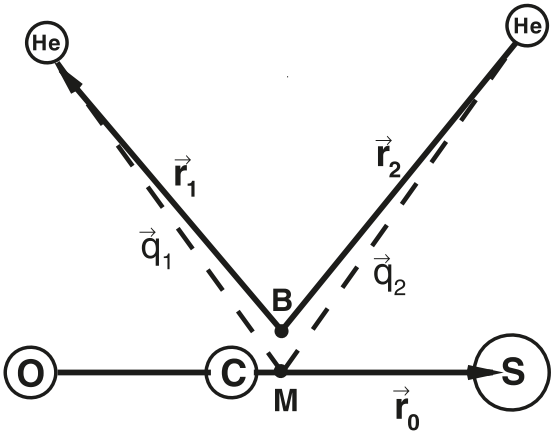

tum calculations on OCS–$(He)_N$ clusters have been restricted to the He–OCS dimer.[18,27] The present paper extends this work to the case of two helium atoms with OCS. In the remainder of this paper, details of the theory and computational procedure are given in the Theory and methods section, results are presented and discussed in the Results and discussion section, and concluding remarks appear in last section.

Theory and methods

General

The methodology used in this work is based mainly on the work of Wang, Carrington, and co-workers[28] and on fundamental ideas presented by Mladenovic.[29] the Wang and Carrington group applied their approach to the N_2O–$(He)_2$ system and were able to reproduce experimentally observable rovibrational transitions quite accurately. Recently, they also applied their approach to CO_2–$(He)_2$ and to CO–$(He)_2$, again with great success.[30,31] The method is briefly reviewed here, and the reader is referred to ref. 28 for further details.

The rovibrational Hamiltonian of the OCS–$(He)_2$ complex in the body-fixed frame has the following form (in au):[28,29,32,33]

$$[1] \qquad \hat{H} = \hat{T}_{\text{str}} + \hat{T}_{\text{diag}} + \hat{T}_{\text{off}} + \hat{T}_{\text{Cor}} + \bar{V}(r_1, r_2, \theta_1, \theta_2, \phi)$$

with

$$[2] \qquad \hat{T}_{\text{str}} = -\frac{1}{2m_{\text{He}}}\frac{\partial^2}{\partial r_1^2} - \frac{1}{2m_{\text{He}}}\frac{\partial^2}{\partial r_2^2}$$

$$[3] \qquad \hat{T}_{\text{diag}} = -\left(\frac{1}{2m_{\text{He}}r_1^2} + B_{\text{OCS}}\right)\left[\frac{\partial^2}{\partial\theta_1} + \cot\theta_1\frac{\partial}{\partial\theta_1} - \frac{1}{\sin^2\theta_1}(\hat{J}_z - \hat{l}_{2z})^2\right] + \left(\frac{1}{2m_{\text{He}}r_2^2} + B_{\text{OCS}}\right)\hat{l}_2^2 + B_{\text{OCS}}[\hat{J}^2 - 2(\hat{J}_z - \hat{l}_{2z})^2 - 2\hat{J}_z\hat{l}_{2z}]$$

$$[4] \qquad \hat{T}_{\text{off}} = B_{\text{OCS}}(\hat{l}_{2+}\hat{a}_1^- + \hat{l}_{2-}\hat{a}_1^+)$$

$$[5] \qquad \hat{T}_{\text{Cor}} = -B_{\text{OCS}}(\hat{J}_-\hat{a}_1^+ + \hat{J}_+\hat{a}_1^- + \hat{J}_-\hat{l}_{2+} + \hat{J}_+\hat{l}_{2-})$$

in which

$$[6] \qquad \hat{J}_\pm = \hat{J}_x \pm i\hat{J}_y, \quad \hat{l}_{2\pm} = \hat{l}_{2x} \pm i\hat{l}_{2y}$$

$$[7] \qquad \hat{a}_1^\pm = \pm\frac{\partial}{\partial\theta_1} - \cot\theta_1(\hat{J}_z - \hat{l}_{2z})$$

Details of the coordinate system are presented in Fig. 1, where r_1 and r_2 are the lengths of Radau (or orthogonalized satellite) vectors $\mathbf{r}_1$ and $\mathbf{r}_2$, which are linear combinations of the Jacobi (or satellite) vectors $\mathbf{q}_1$ and $\mathbf{q}_2$ from the centre of mass of OCS to the He atoms.[29] The polyspherical angles (θ_1, θ_2, and ϕ) are determined by the three vectors ($\mathbf{r}_0$, $\mathbf{r}_1$, and $\mathbf{r}_2$), where $\mathbf{r}_0$ is a vector along the axis of OCS, m_{He} is the mass of the He atom, and B_{OCS} is the inertial rotation constant of OCS. The operators $\hat{J}_x$, $\hat{J}_y$, and $\hat{J}_z$ are the components of the total angular momentum operator $\hat{J}$ in the body-fixed frame, the z axis of the body-fixed frame lies along the Jacobi radial vector $\mathbf{r}_0$, and its x axis is in the plane that contains the vector $\mathbf{r}_0$ and one He atom. $\bar{V}(r_1, r_2, \theta_1, \theta_2, \phi)$ is the total potential represented as a sum of two He–OCS potentials plus the He–He intermolecular potential. The above Hamiltonian contains full vibration–rotation coupling.

Basis function and matrix elements

A discrete variable representation (DVR) grid[34] is used for the radial degree of freedom, while parity-adapted rovibrational basis functions are used for the angular part. The latter are linear combinations of the functions

$$[8] \qquad \langle\theta_1, \theta_2, \phi; \alpha, \beta, \gamma | l_1, l_2, m_2; J, K, M\rangle = \sqrt{\frac{2J+1}{8\pi^2}}\Theta_{l_1}^{K-m_2}(\theta_1)Y_{l_2}^{m_2}(\theta_2, \phi)D_{M,K}^{J^*}(\alpha, \beta, \gamma)$$

with

$$[9] \qquad Y_{l_2}^{m_2}(\theta_2, \phi) = \frac{1}{\sqrt{2\pi}}\Theta_{l_2}^{m_2}(\theta_2)e^{im_2\phi}$$

where $\Theta_l^{m_2}$, $Y_l^{m_2}$, and $D_{M,K}^J$ are, respectively, the normalized associated Legendre function with the $(-1)^{m_2}$ Condon–Shortley phase factor,[35] spherical harmonic functions, and Wigner functions.[35] The body-fixed frame is related to the space-fixed frame via a rotation in the three Euler angles (α, β, γ). The projection of the total angular momentum J onto the space-fixed or body-fixed frame is given by M or K. Applying the parity operator $\hat{E}^*$ to the rovibrational function has the effect

$$[10] \qquad \widehat{E}^{*}|l_1, l_2, m_2, K; J, M\rangle = (-1)^J|l_1, l_2, -m_2, -K; J, M\rangle$$

Parity-adapted basis functions may be written as

$$[11] \qquad |l_1, l_2, m_2, K; J, M, P\rangle = \frac{1}{\sqrt{2(1+\delta_{m_2,0}\delta_{K,0})}}|l_1, l_2, m_2, K; J, M\rangle + (-1)^{J+P}|l_1, l_2, -m_2, -K; J, M\rangle$$

where $K \geq 0$ and $P = 0$ or 1 correspond to even or odd parities, respectively. When $K = 0$ the constraint $m_2 \geq 0$ holds and the combination $m_2 = K = 0$ and $(-1)^{J+P} = -1$ is not allowed.

In the parity-adapted angular finite basis representation(FBR), the kinetic energy terms have simple matrix elements. The diagonal matrix elements are

$$[12] \qquad \langle l_1, l_2, m_2, K; J, M, P|\widehat{T}_{\text{diag}}|l_1, l_2, m_2, K; J, M, P\rangle = \frac{1}{2m_{\text{He}}r_1^2}l_1(l_1+1) + \frac{1}{2m_{\text{He}}r_2^2}l_2(l_2+1) + B_{\text{OCS}}l_1(l_1+1) + B_{\text{OCS}}[J(J+1) + l_1(l_1+1) + l_2(l_2+1) - 2K^2 + 2m_2(K-m_2)]$$

and the three types of off-diagonal matrix elements are

$$[13] \qquad \langle l_1, l_2, m_2+1, K; J, M, P|\widehat{T}_{\text{off}}|l_1, l_2, m_2, K; J, M, P\rangle = \sqrt{1+\delta_{m_2,0}\delta_{K,0}}B_{\text{OCS}}\lambda^{-}_{l_1,K-m_2}\lambda^{+}_{l_2,m_2}$$

$$[14] \qquad \langle l_1, l_2, m_2, K+1; J, M, P|\widehat{T}_{\text{Cor}}|l_1, l_2, m_2, K; J, M, P\rangle = -\sqrt{1+\delta_{m_2,0}\delta_{K,0}}B_{\text{OCS}}\lambda^{+}_{l_1,K-m_2}\lambda^{+}_{J,K}$$

$$[15] \qquad \langle l_1, l_2, m_2+1, K+1; J, M, P|\widehat{T}_{\text{Cor}}|l_1, l_2, m_2, K; J, M, P\rangle = -\sqrt{1+\delta_{m_2,0}\delta_{K,0}}B_{\text{OCS}}\lambda^{+}_{l_2,m_2}\lambda^{+}_{J,K}$$

with two special cases

$$[16] \qquad \langle l_1, l_2, -m_2, 1; J, M, P|\widehat{T}_{\text{Cor}}|l_1, l_2, m_2, 0; J, M, P\rangle = -(-1)^{J+P}B_{\text{OCS}}\lambda^{-}_{l_1,K-m_2}\lambda^{-}_{J,0} \qquad (m_2 > 0)$$

$$[17] \qquad \langle l_1, l_2, -m_2+1, 1; J, M, P|\widehat{T}_{\text{Cor}}|l_1, l_2, m_2, 0; J, M, P\rangle = -(-1)^{J+P}B_{\text{OCS}}\lambda^{-}_{l_2,m_2}\lambda^{-}_{J,0} \qquad (m_2 > 0)$$

where

$$\lambda^{\pm}_{l,m} = \sqrt{l(l+1) - m(m\pm 1)}$$

While the potential is not diagonal in the angular FBR, its matrix element integrals can be calculated in a grid representation via a three-dimensional transformation[36] for the θ_1, θ_2, and ϕ angles.[28,36] A Gauss–Legendre quadrature was used for the θ_1 and θ_2 angles, and Gauss–Chebyshev quadratures of the first and second kind were used to integrate ϕ for even and odd parity cases, respectively. For $J > 0$, a Fourier transform method has been used for potential matrix–vector products.[28,37] The Lanczos algorithm was then used to calculate the rovibrational energy levels by recursively diagonalizing the discretized Hamiltonian matrix.[38–40] Projection operator techniques were used in combination with the Lanczos iteration method to compute symmetric states upon identical helium exchanges to properly account for the bosonic nature of the ^{4}He atoms. This corresponds to a version of the symmetry-adapted Lanczos (SAL) algorithm[41,42] previously used for atomic trimers containing two or more bosonic atoms.[28,43,44] Eigenvectors were obtained using a second Lanczos recursion to avoid the storage of Lanczos vectors as previously done in ref. 43.

Helium density in the body-fixed frame

To develop some intuitive feeling regarding the nature of these species, it is very useful to develop a three-dimensional representation of the helium part of the wave function in the body-fixed frame. In terms of the basis functions and Radau coordinate system, the wave function for the nth energy level for a given set of J, M, and P quantum numbers is

$$[18] \qquad \Psi_n^{J,M,P}(r_1, r_2, \theta_1, \theta_2, \phi; \alpha, \beta, \gamma) = \sum_{\alpha_1,\alpha_2,l_1,l_2,m_2,K} \langle \theta_1, \theta_2, \phi; \alpha, \beta, \gamma|l_1, l_2, m_2, ; J, K, M, P\rangle\langle r_1|\alpha_1\rangle\langle r_2|\alpha_2\rangle \times \langle \alpha_1, \alpha_2, l_1, l_2, m_2; J, K, M, P|\Psi_n^{J,M,P}\rangle$$

in which $\langle r_j|\alpha_j\rangle$ is a localized DVR basis function for helium atom j, and the coefficient $\langle \alpha_1, \alpha_2, l_1, l_2, m_2; J, K, M, P|\Psi_n^{J,M,P}\rangle$ is an eigenvector obtained via Lanczos diagonalization.

The three-dimensional density of the jth helium atom associated with $\Psi_n^{J,M,P}$ is defined as

$$[19] \qquad \rho_j^{J,M,P,n}(\mathbf{R}) = \int \mathrm{d}r_1\mathrm{d}r_2\sin\theta_1\mathrm{d}\theta_1\sin\theta_2\mathrm{d}\theta_2\mathrm{d}\phi|\Psi_n^{J,M,P}(r_1, r_2, \theta_1, \theta_2, \phi; \alpha, \beta, \gamma)|^2\ \delta(\mathbf{R} - \mathbf{R}_j[r_1, r_2, \theta_1, \theta_2, \phi])$$

in which $\mathbf{R}_j[r_1, r_2, \theta_1, \theta_2, \phi]$ is the vector function that maps the Radau coordinates to the body-fixed Cartesian coordinates

Table 1. Calculated energies (in cm^{-1}) for the lowest rotational sublevels of the ground vibrational level for seven OCS–He_2 isotopologues.

	Calculated energy (cm^{-1})			
	Level (J, P, n)			
Isotopologues	0 (0, 0, 0)	1 (1, 1, 0)	2 (2, 0, 0)	3 (3, 1, 0)
$^{16}O^{12}C^{32}S$	–37.9505	–37.6994	–37.2200	–36.5363
$^{16}O^{13}C^{32}S$	–37.9780	–37.7277	–37.2495	–36.5674
$^{16}O^{12}C^{34}S$	–38.0512	–37.8047	–37.3327	–36.6585
$^{16}O^{13}C^{34}S$	–38.0821	–37.8362	–37.3649	–36.6914
$^{16}O^{12}C^{33}S$	–38.0021	–37.7534	–37.2778	–36.5989
$^{18}O^{12}C^{32}S$	–38.1526	–37.9125	–37.4508	–36.7893
$^{17}O^{12}C^{32}S$	–38.0556	–37.8103	–37.3400	–36.6677

Note: J, total angular momentum; P, parity; and n, vibrational quantum number.

Table 2. Comparison of predicted and observed rotational transitions energies of OCS–He_2 isotopologues (in cm^{-1}).

		Rotational transition energy (cm^{-1})		Theory – Expt.	
Isotopologue	$J' \leftarrow J$	Theory	Expt.[3,6]	cm^{-1}	% Diff.
$^{16}O^{12}C^{32}S$	1 ← 0	0.2511	0.252 329	–0.0013	–0.5
	2 ← 1	0.4794	0.478 473	0.0010	0.2
	3 ← 2	0.6837	0.679 346	0.0044	0.6
	$\Delta\nu_t$	0.4510	—		
$^{16}O^{13}C^{32}S$	1 ←0	0.2503	0.25 2064	–0.0017	–0.7
	2 ←1	0.4782	0.478 130	0.0001	0.0
	3 ←2	0.6821	0.678 995	0.0031	0.5
	$\Delta\nu_t$	0.4486	—		
$^{16}O^{12}C^{34}S$	1 ← 0	0.2465	0.246 883	–0.0004	–0.2
	2 ← 1	0.4720	0.470 301	0.0017	0.4
	3 ← 2	0.6742			
	$\Delta\nu_t$	0.4412	—		
$^{16}O^{13}C^{34}S$	1 ← 0	0.2460	0.246 584	–0.0006	–0.3
	2 ← 1	0.4713	0.469 894	0.0013	0.3
	3 ← 2	0.6735	—		
	$\Delta\nu_t$	0.4417	—		
$^{16}O^{12}C^{33}S$	1 ← 0	0.2487	0.249 531	–0.0008	–0.3
	2 ← 1	0.4756	—		
	3 ← 2	0.6789	—		
	$\Delta\nu_t$	0.4459	—		
$^{18}O^{12}C^{32}S$	1 ← 0	0.2401	—		
	2 ← 1	0.4617	—		
	3 ← 2	0.6615	—		
	$\Delta\nu_t$	0.4328	—		
$^{17}O^{12}C^{32}S$	1 ← 0	0.2453	—		
	2 ← 1	0.4703	—		
	3 ← 2	0.6723	—		
	$\Delta\nu_t$	0.4413	—		

Note: All of the observed transitions were a-type between levels within the $K_a = 0$ stack. $\Delta\nu_t$ is the transition energy between the first excited and ground torsion states of He_2 in OCS–He_2 complexes. J, total angular momentum.

($\mathbf{R}j = \{x_j, y_j, z_j\}$). The above integral can be evaluated on the same grid as the potential integral. However, because of the discrete nature of the Gaussian quadrature grid used for the integration, the density may not appear to be smooth. To obtain a smooth representation of the density, we use a Gaussian representation of the three-dimensional delta function that appears in eq. [19]

Table 3. Comparison of predicted and observed spectroscopic constants (in MHz) of OCS–He_2 isotopologues.

Isotopologue	Rotational constants	Spectroscopic constant		Theory – Expt.	
		Theory	Expt.[6]	MHz	% Diff.
$^{16}O^{12}C^{32}S$	*A*	5104.99(14)	5169.6746	–64.6846	–1.25
	B	4308.556(17)	4385.6366	–77.0806	–1.76
	C	3235.885(18)	3195.6404	40.2446	1.26
$^{16}O^{13}C^{32}S$	*A*	5107.05(35)	5741.2483	–634.1983	–11.05
	B	4293.006(42)	4522.5175	–229.5115	–05.08
	C	3227.451(45)	3035.8419	191.6091	06.31
$^{16}O^{12}C^{34}S$	*A*	5018.0(10)	—		
	B	4208.66(12)	—		
	C	3197.88(13)	—		
$^{16}O^{13}C^{34}S$	*A*	5007.1(15)	—		
	B	4194.38(16)	—		
	C	3195.86(18)	—		
$^{16}O^{12}C^{33}S$	*A*	5069.81(59)	—		
	B	4257.462(69)	—		
	C	3215.390(74)	—		
$^{18}O^{12}C^{32}S$	*A*	4873.6(61)	—		
	B	4062.90(64)	—		
	C	3150.95(74)	—		
$^{17}O^{12}C^{32}S$	*A*	4997.7(19)	—		
	B	4180.55(21)	—		
	C	3190.89(24)	—		

Fig. 2. Reduced rotational transition energy plot for $^{16}O^{12}C^{32}S$–$(He)_2$.

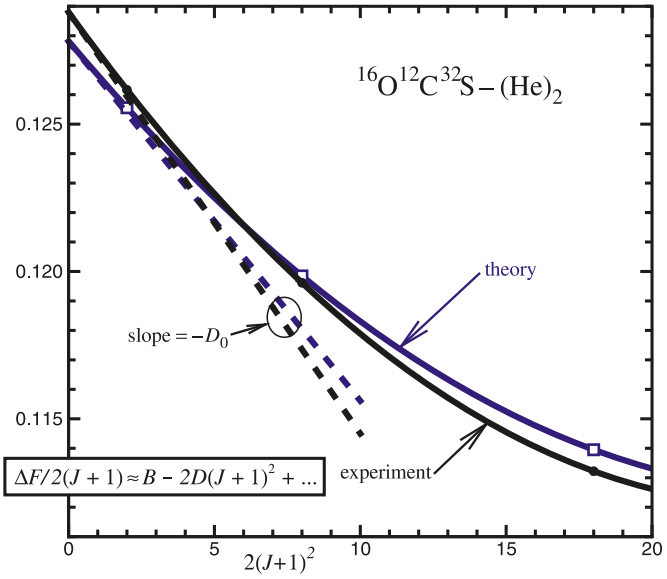

Fig. 3. Three-dimensional representation of the helium-atom density in the body-fixed frame. The position of the first helium defines the location of the *zx* plane, and its density is shown in black, whereas the density of the second He atom is shown in blue. These results were obtained with the values of the Gaussian standard deviations defining the densities set at $\sigma_x = \sigma_z = 0.25$ Å and $\sigma_y = 0.1$ Å for atom–1 and $\sigma_x = \sigma_y = \sigma_z = 0.25$ Å for atom–2.

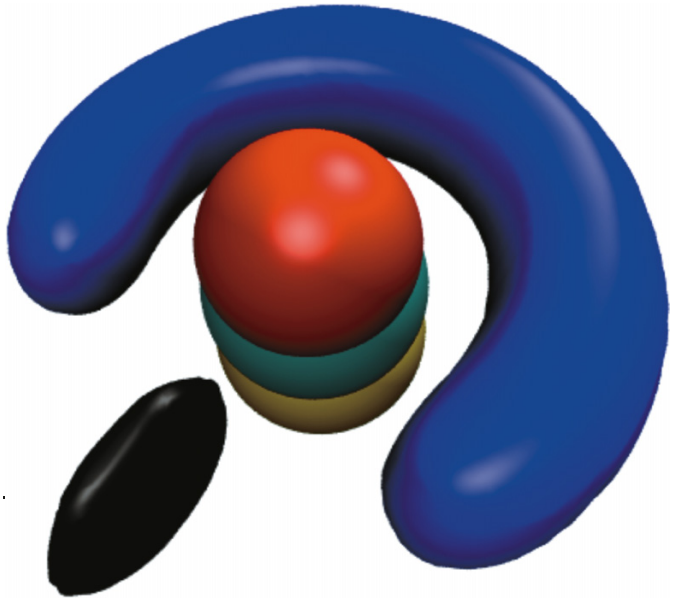

$$[20] \quad \delta(\mathbf{R} - \mathbf{R}_j[r_1, r_2, \theta_1, \theta_2, \phi]) \approx \frac{1}{(2\pi)^{3/2}\sigma_x\sigma_y\sigma_z} e^{(x-x_i)^2/2\sigma_x^2} e^{(y-y_i)^2/2\sigma_y^2} e^{(z-z_i)^2/2\sigma_z^2}$$

This expression reduces to an exact delta function in the limit where $(\sigma_x, \sigma_y, \sigma_z) \rightarrow (0, 0, 0)$. Using such a representation of the delta function amounts to performing a Gaussian binning of the density and leads to a smooth representation of the density, as will be illustrated in the following.

Fig. 4. As in Fig. 3, but with $\sigma_x = \sigma_z = 0.1$ Å and $\sigma_y = 0.05$ Å for atom–1 and $\sigma_x = \sigma_y = \sigma_z = 0.1$ Å for atom–2.

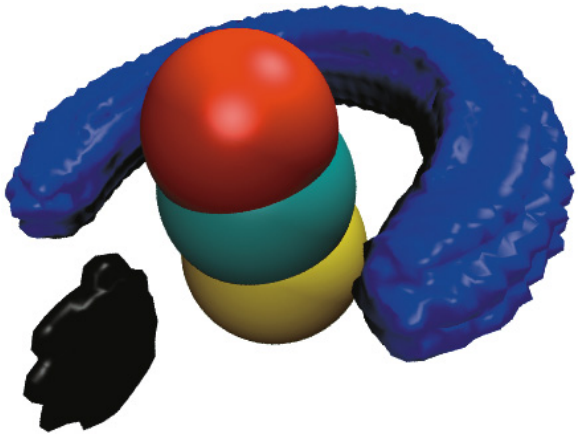

Fig. 5. He-atom density as a function of the azimuthal angle ϕ.

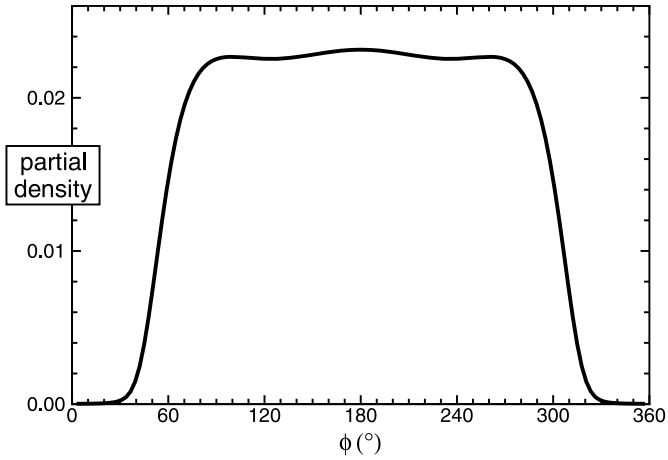

Results and discussion

Bound-state energies and microwave spectrum

The rovibrational energy levels of seven isotopologues of the OCS–$(He)_2$ complex were calculated using the radial DVR and parity-adapted angular FBR methods described in the Theory and methods section. The inertial rotational constants B_{OCS} required for these calculations were fixed at the experimental values of 0.202 856 741 cm^{-1} for $^{16}O^{12}C^{32}S$, 0.202 204 019 cm^{-1} for $^{16}O^{13}C^{32}S$, 0.197 898 033 cm^{-1} for $^{16}O^{12}C^{34}S$, 0.197 194 087 cm^{-1} for $^{16}O^{13}C^{34}S$, 0.200 302 07 cm^{-1} for $^{16}O^{12}C^{33}S$, 0.190 293 341 cm^{-1} for $^{18}O^{12}C^{32}S$, and 0.196 258 106 cm^{-1} for $^{17}O^{12}C^{32}S$[45–47] and the masses were set at 4.002 603 24 u for ^4He, 15.994 914 635 u for ^{16}O, 16.999 131 5 u for ^{17}O, 17.999 160 3 u for ^{18}O, 12 u for ^{12}C, 13.003 354 826 u for ^{13}C, 31.972 070 70 u for ^{32}S, 32.971 458 43 u for ^{33}S, and 33.967 866 65 u for ^{34}S. The He–OCS and He–He potentials were taken from refs. 27 and 48, respectively. For r_1 and r_2, 35 sine DVR basis functions were used on the domain 3.0–19.0 b. For the angular basis, $l_{max} = m_{max} = 25$, and 30 Gauss–Legendre quadrature points were used for each of θ_1 and θ_2, while 64 equally spaced points on the range $[0, 2\pi]$ were used for ϕ. To accelerate the convergence of the Lanczos calculation, an energy ceiling of 1000 cm^{-1} was imposed. This energy cutoff affected the low-lying levels by less than 0.001 cm^{-1}.

The energies of the $J = 0$, 1, 2, and 3 rotational sublevels of the ground vibrational level for seven OCS–$(He)_2$ isotopologues are listed in Table 1, where P is the total parity. As shown there, the binding energy of the ground vibrational level of $^{16}O^{12}C^{32}S$–$(He)_2$ is 37.9505 cm^{-1}, which is approximately one-third of the total three-body well depth of 108.0896 cm^{-1}. Because of our additive model, this well depth is exactly twice the 50.22 cm^{-1} well depth[27] of He–OCS plus the 7.6496 cm^{-1} depth of the He–He potential.[48] However, this ground-state level is bound by 0.6993 cm^{-1} *more* than the twice the binding energy of the He–OCS dimer (18.625 cm^{-1})[27] plus the binding energy of the helium dimer (0.0012 cm^{-1}),[48], which add up to 37.2512 cm^{-1}. That additive value is expected to be approximate because it neglects the effect of correlation associated with the mixing of the two He-atom wave functions.

Table 2 compares our calculated microwave transition energies with the experimental results of refs. 3 and 6. As shown there, the agreement is quite good, as the relative errors are never larger than 0.7%. The $\Delta\nu_t$ torsional frequency values are also presented in Table 2. For additional comparison, the calculated microwave transitions were fitted to Watson's S-reduction Hamiltonian as an asymmetric top molecule and compared to the experimental results of ref. 6. All resulting spectroscopic constants are listed in Table 3. As shown in Table 3 for $^{16}O^{12}C^{32}S$–$(He)_2$, the fitted A, B, and C rotational constants agree well with experimental results, as the relative errors are less than 2%. However, for $^{16}O^{13}C^{32}S$–$(He)_2$, the errors are relatively larger than those of $^{16}O^{12}C^{32}S$–$(He)_2$ isotopomer. This is in part due to the fact that the centrifugal distortion constants for all isotopologues were fixed to the same infrared value[7] of $^{16}O^{12}C^{32}S$–$(He)_2$. Another explanation for the discrepancy is the neglect of three-body terms in the interaction potential used in the calculations as discussed below.

It is evident that the J dependence of the residual discrepancies in Table 2 has the same systematic behaviour for all isotopologues: the theoretical $1 \leftarrow 0$ transition frequencies are smaller than the experimental ones, whereas the experimental transition frequencies are larger in the $3 \leftarrow 2$ and $2 \leftarrow 1$ cases. This behaviour can be understood if we use a basic spectroscopic analysis to determine estimates of the leading rotational constants implied by these results. In particular, according to a standard spectroscopic analysis in which rotational energies are written as $F(J) = B_v[J(J+1)] - D_v[J(J+1)]^2 + \ldots$, the expression for the rotational transition energies $\Delta F(J) \equiv F(J+1) - F(J)$ may be rearranged into the form

$$[21] \qquad \frac{\Delta F(J)}{2(J+1)} = B_v - 2D_v(J+1)^2 + 3H_v[(J+1)^2(J^2+2J+2)]\cdots$$

Plots of the experimental and theoretical results for $^{16}O^{12}C^{32}$–He in the manner suggested by eq. [21] are presented in Fig. 2; the intercepts of these plots indicate the values of the inertial rotational constants B_v and the slopes the values of the leading centrifugal distortion constant D_v. The 0.77% difference between the experimental and theoretical B_v values and 17% difference between the corresponding

D_v. values are orders of magnitude larger than the discrepancies implied by the differences between the experimental and theoretical results for He–OCS obtained by Howson and Hutson.[27] Since our calculations are based on their He–OCS pair potential, and given that the He–He pair potential[48] is believed to be very reliable, we interpret these differences as being due to our neglect of nonadditive contributions to the overall interaction potential of our three-body system. The fact that the experimental values are larger than those obtained from our additive model would be consistent with the existence of an attractive three-body interaction.

Helium density

Figures 3 and 4 present the three-dimensional density for the two helium atoms in the body-fixed frame as calculated for the ground state of OCS–$(He)_2$ using the procedure described in the Helium density in the body-fixed frame section. Iso-surfaces are used to represent the three-dimensional densities, and the z axis is defined to lie on the OCS molecular axis. The density of helium atom–1 is represented in black and that of helium atom–2 is shown in blue. Two sets of standard deviation parameters have been chosen to illustrate the smearing effect of the Gaussian binning. Larger values of $\sigma_x = \sigma_z = 0.25$ Å and $\sigma_y = 0.1$ Å for atom–1 and $\sigma_x = \sigma_y = \sigma_z = 0.25$ Å for atom–2 are used in Fig. 3, whereas smaller values of $\sigma_x = \sigma_z = 0.1$ Å and $\sigma_y = 0.05$ Å for atom–1 and $\sigma_x = \sigma_y = \sigma_z = 0.1$ Å for atom–2 are used in Fig. 4. We first observe that a smoother density is obtained with the larger standard deviation parameters, although the general features of the helium density are the same in both Figs. 3 and 4. The density will be accurately represented as long as the standard deviations are smaller than the characteristic length scale of the features of the wave function. The values chosen above obey this criterion.

One significant feature of these representations is the fact that the two helium atoms appear to have very different density distributions. This is an artifact of the fact that the position of helium atom–1 is used *to define* the xz plane of the body-fixed frame, and its density is therefore completely localized with respect to the y direction. Indeed, the only reason that its density distribution appears to have nonzero width in the y direction (the thickness of the black "disk") is the use of a finite bin size ($\sigma_y > 0$) in the calculation. The density of helium atom–1 is of course somewhat delocalized in the xz plane, but it is centred at the minimum of the potential energy surface.

The second helium atom is clearly highly delocalized relative to the first, being distributed on a "sausage"-shaped incomplete ring about the OCS molecule axis. In Figs. 3 and 4 it appears to have a uniform density as a function of the azimuthal angle ϕ, apart from the region near atom–1 whence it is excluded by the short-range repulsive wall of the He–He potential. However, Fig. 5 shows that the "partial density" obtained by integrating the density of He atom–2 with respect to R and z at each value of ϕ has interesting substructure. In particular, in addition to the expected excluded volume near $\phi = 0^\circ$ and 360°, there are small but distinct local maxima at $\phi = 101^\circ$ and 259° corresponding to the two He atoms lying ~5.4 Å apart. This distance is almost double the He–He potential equilibrium distance of r_e = 2.968 Å, but is much smaller than the 45.6 Å expectation value of the internuclear distance in the ground state of an isolated He_2 molecule, since the relatively strong He–OCS potential constrains the two He atoms to lie within a ring about the axis of the OCS. However, the weakness of the He–He potential means that over a ϕ range of almost 180° the two He atoms move almost freely relative to one another. Note that the present structural analysis is consistent with Fig. 2 of ref. 49, and the findings of Wang and Carrington and co-workers for the related He_2–N_2O.[28]

Concluding remarks

Calculated rovibrational energy levels and microwave transitions for seven OCS–$(He)_2$ isotopologues have been obtained from using a global potential energy surface defined as a sum of accurate He–OCS and He–He pair potentials. The predicted microwave transitions are in fairly good agreement with experiment, but small systematic residual differences are attributed to our neglect of three-body contributions to the interaction. A new approach for visualizing the helium density in the body-fixed frame is introduced that shows that for the ground state, relative to the first, the second helium atom lies in a sausage-shaped incomplete ring about the OCS axis, with a region of excluded density owing to the helium–helium repulsion. This study is complementary to one by Wang and Carrington,[49] for this same OCS–$(He)_2$ system in the August 2010 issue of this journal — they focus more on the infrared spectra and the intramolecular vibrational structure and consider only the most abundant isotopologues. Although they use different interaction potentials, their results are in general agreement with ours.

Acknowledgments

The authors thank Professor T. Carrington, Jr. and Dr. X.-G. Wang for helpful discussions. Drs. H.-G. Yu and N. Blinov are also gratefully acknowledged for useful suggestions. This research has been supported by the Natural Sciences and Engineering Research Council of Canada (NSERC), the Canada Foundation for Innovation (CFI), and the University of Waterloo. We thank the Shared Hierarchical Academic Research Computing Network (SHARCNET) for computing time.

References

(1) Grebenev, S.; Toennies, J. P.; Vilesov, A. F. *Science* **1998**, *279* (5359), 2083. doi:10.1126/science.279.5359.2083. PMID:9516103.
(2) Toennies, J. P.; Vilesov, A. F. *Annu. Rev. Phys. Chem.* **1998**, *49* (1), 1. doi:10.1146/annurev.physchem.49.1.1. PMID: 15012423.
(3) Xu, Y.; Jäger, W. *Chem. Phys. Lett.* **2001**, *350* (5-6), 417. doi:10.1016/S0009-2614(01)01314-8.
(4) Tang, J.; Xu, Y.; McKellar, A. R. W.; Jäger, W. *Science* **2002**, *297* (5589), 2030. doi:10.1126/science.1073718. PMID:12242436.
(5) Tang, J.; McKellar, A. R. W. *J. Chem. Phys.* **2003**, *119* (2), 754. doi:10.1063/1.1578473.
(6) Xu, Y.; Jäger, W. *J. Chem. Phys.* **2003**, *119* (11), 5457. doi:10.1063/1.1598953.

(7) Tang, J.; McKellar, A. R. W. *J. Chem. Phys.* **2003**, *119* (11), 5467. doi:10.1063/1.1598954.
(8) Tang, J.; McKellar, A. R.; Mezzacapo, F.; Moroni, S. *Phys. Rev. Lett.* **2004**, *92* (14), 145503. doi:10.1103/PhysRevLett.92.145503. PMID:15089550.
(9) Tang, J.; McKellar, A. R. W. *J. Chem. Phys.* **2004**, *121* (1), 181. doi:10.1063/1.1758701. PMID:15260536.
(10) McKellar, A. R. *J. Chem. Phys.* **2007**, *127* (4), 044315. doi:10.1063/1.2756537. PMID:17672698.
(11) McKellar, A. R.; Xu, Y.; Jäger, W. *J. Phys. Chem. A* **2007**, *111* (31), 7329. doi:10.1021/jp070618w. PMID:17455923.
(12) McKellar, A. R. W. *J. Chem. Phys.* **2008**, *128* (4), 044308. doi:10.1063/1.2822903. PMID:18247950.
(13) Surin, L. A.; Potapov, A. V.; Dumesh, B. S.; Schlemmer, S.; Xu, Y.; Raston, P. L.; Jäger, W. *Phys. Rev. Lett.* **2008**, *101* (23),o. 233401. doi:10.1103/PhysRevLett.101.233401. PMID:19113549.
(14) Paesani, F.; Gianturco, F. A.; Whaley, K. B. *J. Chem. Phys.* **2001**, *115* (22), 10225. doi:10.1063/1.1412873.
(15) Paesani, F.; Viel, A.; Gianturco, F. A.; Whaley, K. B. *Phys. Rev. Lett.* **2003**, *90* (7), 073401. doi:10.1103/PhysRevLett.90.073401.
(16) Paesani, F.; Whaley, K. B. *J. Chem. Phys.* **2004**, *121* (9), 4180. doi:10.1063/1.1768931. PMID:15332966.
(17) Moroni, S.; Sarsa, A.; Fantoni, S.; Schmidt, K. E.; Baroni, S. *Phys. Rev. Lett.* **2003**, *90* (14), 143401. doi:10.1103/PhysRevLett.90.143401. PMID:12731914.
(18) Blinov, N.; Song, X.-G.; Roy, P.-N. *J. Chem. Phys.* **2004**, *120* (13), 5916. doi:10.1063/1.1650301. PMID:15267473.
(19) Paolini, S.; Fantoni, S.; Moroni, S.; Baroni, S. *J. Chem. Phys.* **2005**, *123* (11), 114306. doi:10.1063/1.2032969. PMID:16392558.
(20) Li, H.; Blinov, N.; Roy, P.-N.; Le Roy, R. J. *J. Chem. Phys.* **2009**, *130* (14), 144305. doi:10.1063/1.3109897. PMID:19368443.
(21) Blinov, N.; Roy, P.-N. *ACS Symp. Ser.* **2007**, *953*, 165. doi:10.1021/bk-2007-0953.ch012.
(22) Moroni, S.; Blinov, N.; Roy, P.-N. *J. Chem. Phys.* **2004**, *121* (8), 3577. doi:10.1063/1.1774160. PMID:15303924.
(23) Xu, Y. J.; Blinov, N.; Jäger, W.; Roy, P. N. *J. Chem. Phys.* **2006**, *124* (8), 081101. doi:10.1063/1.2173640. PMID:16512695.
(24) Blinov, N.; Roy, P.-N. *J. Low Temp. Phys.* **2005**, *140* (3–4), 253. doi:10.1007/s10909-005-6312-y.
(25) Paesani, F.; Kwon, Y.; Whaley, K. B. *Phys. Rev. Lett.* **2005**, *94* (15), 153401. doi:10.1103/PhysRevLett.94.153401. PMID:15904142.
(26) Topic, W.; Jäger, W.; Blinov, N.; Roy, P. N.; Botti, M.; Moroni, S. *J. Chem. Phys.* **2006**, *125* (14), 144310. doi:10.1063/1.2357604. PMID:17042593.
(27) Howson, J. M. M.; Hutson, J. M. *J. Chem. Phys.* **2001**, *115* (11), 5059. doi:10.1063/1.1394940.
(28) Wang, X.-G.; Carrington, T., Jr.; Tang, J.; McKellar, A. R. *J. Chem. Phys.* **2005**, *123* (3), 034301. doi:10.1063/1.1924408. PMID:16080731.
(29) Mladenović, M. *J. Chem. Phys.* **2000**, *112* (3), 1070. doi:10.1063/1.480662.
(30) Tang, J.; McKellar, A. R. W.; Wang, X. G.; Carrington, T., Jr. *Can. J. Phys.* **2009**, *87* (5), 417. doi:10.1139/P08-119.
(31) Wang, X.-G.; Carrington, T., Jr.; McKellar, A. R. W. *J. Phys. Chem. A* **2009**, *113* (47), 13331. doi:10.1021/jp904778f. PMID:19842654.
(32) Gatti, F.; Iung, C.; Menou, M.; Justum, Y.; Nauts, A.; Chapuisat, X. *J. Chem. Phys.* **1998**, *108* (21), 8804. doi:10.1063/1.476327.
(33) Yu, H.-G. *Chem. Phys. Lett.* **2002**, *365*, 189. doi:10.1016/S0009-2614(02)01453-7.
(34) Light, J. C.; Hamilton, I. P.; Lill, J. V. *J. Chem. Phys.* **1985**, *82* (3), 1400. doi:10.1063/1.448462.
(35) Zare, R. N. *Angular Momentum:* Wiley; New York, 1988.
(36) Ying Lin, S.; Guo, H. *J. Chem. Phys.* **2002**, *117* (11), 5183. doi:10.1063/1.1500731.
(37) Wang, X.-G.; Carrington, T., Jr. *J. Chem. Phys.* **2005**, *123* (15), 154303. doi:10.1063/1.2043148. PMID:16252944.
(38) Lanczos, C. *J. Res. Natl. Bur. Stand.* **1950**, *45*, 255.
(39) Golub, G. H.; van Loan, C. F. *Matrix Computations;* Johns Hopkins University Press: Baltimore, 1989.
(40) Cullum, J. K.; Willoughby, R. A. *Lanczos Algorithms for Large Symmetric Eigenvalue Computations:* Birkhäuser: Boston, 1985.
(41) Wang, X.-G.; Carrington, T., Jr. *J. Chem. Phys.* **2001**, *114* (4), 1473. doi:10.1063/1.1331357.
(42) Chen, R.; Guo, H. *J. Chem. Phys.* **2001**, *114* (4), 1467. doi:10.1063/1.1331356.
(43) Roy, P.-N. *J. Chem. Phys.* **2003**, *119* (11), 5437. doi:10.1063/1.1599348.
(44) Liu, Y. D.; Roy, P.-N. *J. Chem. Phys.* **2004**, *121* (13), 6282. doi:10.1063/1.1787488. PMID:15446922.
(45) Saupe, S.; Wappelhorst, M. H.; Meyer, B.; Urban, W.; Maki, A. G. *J. Mol. Spectrosc.* **1996**, *175* (1), 190. doi:10.1006/jmsp.1996.0021.
(46) Lahaye, J. G.; Vandenhaute, R.; Fayt, A. *J. Mol. Spectrosc.* **1987**, *123* (1), 48. doi:10.1016/0022-2852(87)90262-1.
(47) Townes, C. H.; Schawlow, A. L. *Microwave Spectroscopy;* McGraw-Hill: New York, 1955.
(48) Jeziorska, M.; Cencek, W.; Patkowski, K.; Jeziorski, B.; Szalewicz, K. *J. Chem. Phys.* **2007**, *127* (12), 124303. doi:10.1063/1.2770721. PMID:17902899.
(49) Wang, X.-G.; Carrington, T., Jr. *Can. J. Chem.* **2010**, *88*, 779. doi:10.1139/v10-030.